Understanding the force motion trade off of rigid and hinged floating platforms for marine renewables.

Abel Arredondo-Galeana, Saishuai Dai, Yongqiang Chen, Xiantao Zhang and Feargal Brennan

Abstract—**In this work, we study the motion and loading response of a very large hinged floating platform. Such platform could host several floating marine renewable devices or alternatively, could extract energy through hinge motion. To this aim, we benchmark the response of a laboratory scale hinged platform to the motion and loading response of a rigid platform subject to regular waves. The hinged structure has two hinges and three pontoons, whilst the rigid structure is equipped with steel bars rather than hinges. The platforms are instrumented with motion detection spheres and the hinge assembly with strain gauges to measure vertical point loads. We find that the motion response of the hinged and rigid platforms is similar when the wavelength of the incoming wave is higher or smaller than the length of the platform. However, when the wavelength is similar to the length of the platform, single and triple sagging deformations occur for the rigid and hinged structures, respectively. In terms of loading response, we find significant load alleviation for the hinged structure when the wavelength is similar to the length of the platform. These insights reveal that very large hinged floating structures can contribute to offshore survivability by reducing loads in the structure. At the same time, the identification of motion behaviours are necessary to select operating configurations for mounted marine renewable devices.**

Index Terms—**Very large floating platform, Floating marine renewable, Structural loads, Motion detection**

I. Introduction

THERE are multiple scenarios where very large floating structures (VLFS) can be of utility. In areas where land is scarce, they can be used to build airports, bridges or islands in the ocean. Alternatively, VLFS can be used as foundations of multiple offshore renewable energy devices to reduce further installation costs [1]–[3]. Therefore, VLFS could help solving some current societal problems, such as demographic growth and sustainable energy generation.

However, the practical implementation of VLFS poses significant engineering challenges. In particular, VLFS are subject to high loading due to large water planes. Therefore, there is a need for creative solutions that can alleviate the internal loading of the structures and reduce the risk of fatigue failure. An example of loading reduction strategies in VLFS is the use of hinges. In fact, recent numerical studies have evaluated the effect of hinges in the motion response and loading of VLFS [1], [2], [4]–[9]. Furthermore, the use of hinges in VLFS can allow wave energy extraction. An example of a hinge mechanism for energy extraction is, for example, the hinged raft of Sir Christopher Cockerell [10], [11]. A structure that is segmented through hinges and converts the relative motion of the segments to energy.

Although, several studies have been carried out to understand the behaviour of hinged VLFS, most studies have used a numerical approach, through the boundary element method (BEM). However, much fewer experimental studies exist on these type of platforms. The few available experimental studies have focused on measuring the motion induced response of hinged platforms [12]. Furthermore, to the best knowledge of the authors of this paper, the loading of rigid and hinged VLFS platforms has not been measured and compared experimentally, and in the context of offshore renewables.

The limited experimental data on hinged VLFS to benchmark numerical studies, and the need to understand their feasibility towards marine renewables, underpins the purpose of this work. Firstly, we aim to validate experimentally the numerical VLFS model of [1], [13], which hydroelastic effect considerations. Secondly, we carry out a comprehensive experimental characterisation of loading and motion performance on the platform, through strain gauges and a motion detection instrumentation, to understand better the scope of applicability to host marine renewable energy devices.

Specifically, we compare the performance of a rigid and hinged VLFS platforms. We identify the motion characteristics of the platforms subject to large, intermediate and short wavelenghts. We quantify the vertical loading on both rigid and hinged structures with strain gauges at the hinged connections. The numerical model is compared to the experimental results. Lastly, we analyse the results in terms of applicability to deploy marine renewable energy devices.

II. Methodology

A. Experimental setup

The VLFS prototype tested in this work is shown in Figure 1 in calm water. The dimensions of the platform

This work was supported by the EPSRC Supergen ORE hub 2018 under grant EP/S000747/1.

A.A.G, S.D. and F.B are with the Department of Naval Architecture, Ocean and Marine Engineering at the University of Strathclyde, Glasgow, UK, (e-mail: abel.arredondo-galeana@strath.ac.uk, saishuai.dai@strath.ac.uk, feargal.brennan@strath.ac.uk).

Y.C. and X.Z. are with the State Key Laboratory of Ocean Engineering, Shanghai Jiao Tong University, Shanghai, China, (e-mail: chen.y.q@sjtu.edu.cn, zhxt@sjtu.edu.cn).

Digital Object Identifier:
https://doi.org/10.36688/ewtec-2023-389

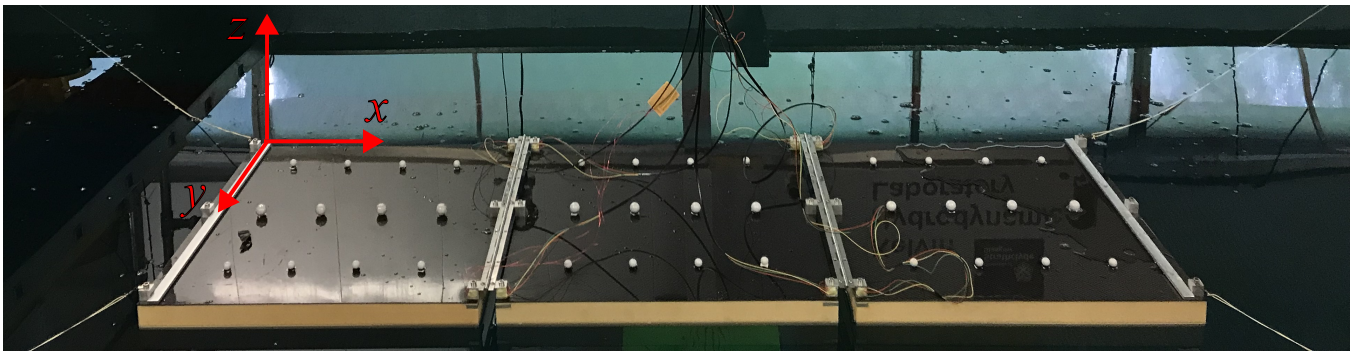

Fig. 1. Image of the VLFS structure in calm water, with body frame of reference showing the x, y and z-axes.

were 1800 mm × 580 mm × 52 mm, with a scale factor of 1:100th with respect to a full scale design. The experimental platform was built with three pontoons connected with two hinges. The gap between pontoons was 30 mm. The hinges were replaced by rigid steel bars to fabricate a rigid version of the floating platform. Stability inserts were installed onboard at the free ends of the VLFS, and inboard at the edges of each pontoon, to level the platform in calm water.

The pontoons were built with two layers of different materials. The top layer was a 2 mm thick carbon fibre sheet with a surface area of $580\,\mathrm{mm} \times 580\,\mathrm{mm}$. The bottom layer consisted of PVC foam, commercially known as Divinycell matrix. The dimensions of the foam were also 580 × 580 mm with a thickness of 50 mm. The total depth of the platform was 52 mm. The draught or submerged part of the platform, in calm water, was 10 mm. Four soft mooring lines were connected at the corners of the VLFS to restrain the motion of the structure. The mooring lines restricted sway, surge, roll and yaw, but allowed heave and pitch motion of the structure. The mooring lines are visible in Figure 1. The lines are tensioned and connected to the corners of the floating platform.

The hinges of the model scale VLFS were off-the-shelf components, commonly known as piano hinges, and were connected to the pontoons with a set of aluminium blocks. A close up of the hinge assembly is shown in Figure 2. The Figure shows the aluminium blocks connected to two pontoons and one hinge. Three aluminium blocks were connected at each side of each hinge, and the blocks were distributed evenly throughout the length of the hinge. The dimensions of the blocks were $1\,\mathrm{cm} \times 1\,\mathrm{cm} \times 1\,\mathrm{cm}$.

The vertical force at the hinge was measured with strain gauges. Each hinge had four strain gauges connected to four of the six aluminium blocks that supported each hinge. The strain gauges were located at the front and back blocks of each hinge. In Figure 2, the front strain gauges can be seen covered with epoxy for water insulation. Due to data throughput limitations, only four strain gauges were available per hinge. Although maximum vertical loads could occur half way of the hinge, the strain gauges were located at the front and back of the hinges to provide redundancy in the measurements in case any of the signals would fail during testing. For the rigid structure, the hinge was replaced with a rigid steel bar, however, the strain gauge assembly remain unaltered. The excitation voltage of each strain gauge was 10 VDC. Signals were recorded and amplified with a multiprocessor data acquisition system. During testing, the cables of the strain gauges were raised over the platform with enough slack to avoid interference with the motion of the platform.

The vertical force on a cross strain gauge, such as the one used in the aluminium block arrangements, can be defined as

$$V = \frac{G\gamma bI}{Q}, \tag{1}$$

where G is the modulus of shear strain, γ is the shear strain, b is the thickness, I is the moment of inertia and Q is the moment of area of the section where the strain gauge is located. For aluminium $G = 28$ GPa and γ is defined as

$$\gamma = 2\epsilon, \tag{2}$$

where ϵ is the strain measured by the strain gauge.

The block was of rectangular cross section, hence, the moment of area Q and the moment of inertia I are defined as

$$Q = \frac{bh^2}{8} \tag{3}$$

and

$$I = \frac{bh^3}{12}. \tag{4}$$

The motion of the platform was measured with a Qualisys system. A total of twelve motion detector spheres per pontoon were used, as illustrated in Figure 1. Five cameras tracked the motion of the spheres, two to the side and three looking down and at the top of the platform. A high resolution camera was also used to record the experimental runs.

The testing facility was the Kelvin Hydrodynamics Laboratory a the University of Strathclyde. The tank is a $76\,\mathrm{m} \times 4.6\,\mathrm{m}$ facility, with a water depth of $2.5\,\mathrm{m}$ and a flat horizontal bed. A photograph of the tank with the VLFS at rest is shown in Figure 3. The tank is equipped with a towing carriage and four wave paddles. The paddles were used to generate the train of regular waves during this experiment. The towing carriage was used to monitor the platform and perform the data acquisition. The carriage was placed in close

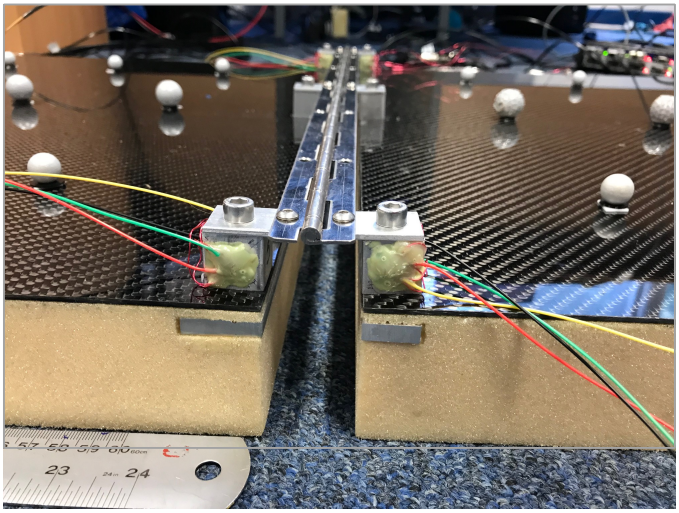

Fig. 2. Hinge assembly showing two of the 6 aluminium blocks with strain gauges covered with epoxy.

proximity to the floating platform, as shown in Figure 3, to allow wired connectivity to the strain gauges.

The floating platform was located half way of the total length of the wave tank. The amplitude of the incoming wave was measured 5 m upstream of the floating platform, with an ultrasonic wave gauge.

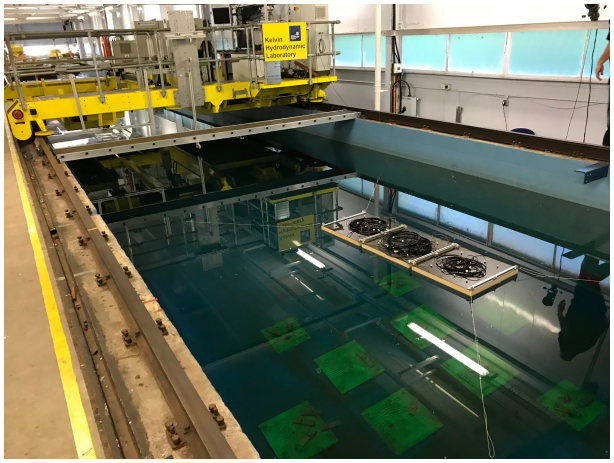

Fig. 3. Kelvin Hydrodynamics Laboratory and floating platform at rest.

B. Hydromechanical model

The hydromechanical model utilised in this work was developed by Zhang et al. [1], [6]. The model estimates the displacements and forces of hinged floating platforms subject to regular waves. In this paper, we present a summary of the assumptions of the model by considering a dual floater with a single hinge assembly. The hydromechanical model consists of two components. The first component consists of multirigid body dynamic assumptions. The second component consists of beam theory and introduces elasticity considerations to the model.

The first row of Figure 4 shows an schematic of a simplified dual module floating platform with a single hinge. The two floaters are depicted as multirigid bodies composed of different segments, as illustrated in the second row of Figure 4. Each segment is represented with a lump mass, and each lump mass is joined with an elastic beam, as indicated in the third row of Figure 4. The number of segments are denoted from 1 to $N_1 + N_2$, where N_1 is the total number of segments of the first floater and N_2 the total number of segments of the second floater.

The displacement vector of each lump mass is denoted as $\zeta^{\mathbf{m}}$, where m denotes the number of the segment from m =1 to N_1+N_2. Each $\zeta^{\mathbf{m}}$ has 6 degrees of freedom, namely, surge, sway, heave, roll, pitch and yaw. Therefore, the total displacement of the full floating structure ζ is a matrix of 6 $\times(N_1+N_2)$ elements.

The forces acting on the lump masses of the segments are the wave excitation force $\mathbf{F}_E$, the added mass force $\omega^2\mathbf{A}(\omega)\zeta$, the radiation damping force, $i\omega\mathbf{B}(\omega)\zeta$, the hydrostatic force -$\mathbf{C}\zeta$ and the inertia force $\omega^2\mathbf{M}\zeta$. Neglecting hydroelastic effects, we can formulate the force equilibrium equation in the system, such that

$$-\omega^2(\mathbf{M}+\mathbf{A}(\omega))\zeta - i\omega\mathbf{B}(\omega)\zeta + \mathbf{C}\zeta = \mathbf{F}_E, \qquad (5)$$

where **A**, **B**, **C** and **M** are the added mass, the radiation damping, the hydrostatic coefficient and the mass matrices, respectively. In Equation (5), the dimensions of matrices **A**, **B**, **C** and **M** are $6(N_1+N_2) \times 6(N_1+N_2)$. While the dimensions of forces $\mathbf{F}_E$, $\omega^2\mathbf{A}(\omega)\zeta$, $i\omega\mathbf{B}(\omega)\zeta$, $\mathbf{C}\zeta$ and $\omega^2\mathbf{M}\zeta$ are 6 $\times(N_1+N_2)$. Further details on the shape of the matrices can be found in [6].

We recall, from Figure 4, that each lump mass is connected to each other through an elastic beam. Hence, the structural deformation induced force is defined as

$$F_S = -K_S\zeta, \qquad (6)$$

where K_S is the stiffness matrix of the full floating platform. Here, K_S is composed by the stiffness matrix of each beam element (K_e) connecting the lump masses of each segment, as described in [1]. Briefly, K_S is made up by assembling each individual K_e into a $6(N_1+N_2) \times 6(N_1+N_2)$ matrix. Then, Equation (6) is incorporated into Equation (5) to account for the structural deformation induced force, such that

$$-\omega^2(\mathbf{M}+\mathbf{A}(\omega))\zeta - i\omega\mathbf{B}(\omega)\zeta + (\mathbf{C}+\mathbf{K}_S)\zeta = \mathbf{F}_E. \qquad (7)$$

The next step in the hydromechanical model is the modelling of motion transfer between the hinge and the floaters. Effectively, only the segments adjacent to the hinge (N_1 and N_1 + 1) influence the motion of the hinge. Figure 5 shows a line segment a-b that represents the hinge, and half the length of segments N_1 and N_1 + 1. We denote the adjacent lump masses as A and B, to the left and right of the hinge, respectively.

Note that in Figure 5, a and b, are two points in the hinge body which are physically connected to the adjacent lump masses A and B. Hence, the motion transfer between a and A, and between b and B can be defined as

$$\zeta_a = \mathbf{L_A}\zeta_A \quad \text{and} \quad \zeta_b = \mathbf{L_B}\zeta_B, \qquad (8)$$

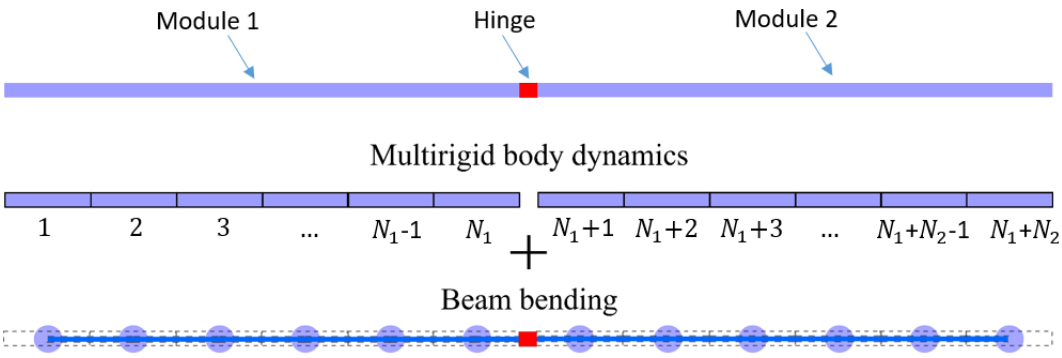

Fig. 4. Schematic representation of two layered block in the floating platform.

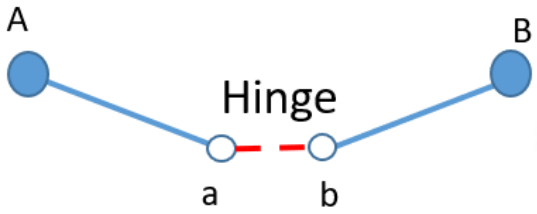

Fig. 5. Schematic representation of motion transfer from segments adjacent to hinge to hinge.

where $\mathbf{L_A}$ and $\mathbf{L_B}$ are Lagrangiang motion transformation matrices between A and a and B and b, respectively, and where ζ_a, ζ_A, ζ_b and ζ_B are the displacement vectors of a, A, b and B, respectively.

Note that in Figure 5, a and b do not pitch, since pitching motion is eliminated due to the presence of the hinge body. Therefore, $\mathbf{L_A}$ and $\mathbf{L_B}$ are matrices of 5×6, where the 6-DOF of A and B, affect only 5-DOF of a and b. Then we can write $\mathbf{L_X}$, as

$$\mathbf{L_X} = \begin{bmatrix} 1 & 0 & 0 & 0 & 0 & 0 \\ 0 & 1 & 0 & 0 & 0 & \left(\frac{L_s}{2} + \frac{L_h}{2}\right) \\ 0 & 0 & 1 & 0 & -\left(\frac{L_s}{2} + \frac{L_h}{2}\right) & 0 \\ 0 & 0 & 0 & 1 & 0 & 0 \\ 0 & 0 & 0 & 0 & 0 & 1 \end{bmatrix} \quad (9)$$

where $\mathbf{X}$ = A or B, L_s is the length of one of the N-the segments of the floaters and L_h is the length of the hinge. Because a and b are both part of the hinge, they are both subject to the same motion displacement, therefore,

$$\zeta_a - \zeta_b = 0. \quad (10)$$

Subsequently, we can express, in matrix form, the influence of the non adjacent and the adjacent segments to the hinge (A and B), to the motion response of a and b, such that

$$\mathbf{\Xi}\zeta = [\mathbf{0} \;\; \mathbf{L_A} \;\; -\mathbf{L_B} \;\; \mathbf{0}]\zeta = 0, \quad (11)$$

where $\mathbf{\Xi}$ is the motion constraint matrix, and $\mathbf{0}$ is a zero matrix of dimensions $5 \times 6(N_1\text{-}6)$.

Lastly, because the forces are considered only in the lump masses of the multibody floater, the forces acting on the hinge $\mathbf{F_J}$ are displaced to the adjacent lump masses, A and B, with the transpose of $\mathbf{\Xi}$, such that

$$\mathbf{\Xi^T F_J}, \quad (12)$$

where $\mathbf{F_J}$ is an unknown vector of 6×1 dimensions and $\mathbf{\Xi}^T$ is the transpose of $\mathbf{\Xi}$. Combining Equations (7), (11) and (12), we can write

$$\begin{bmatrix} -\omega^2(\mathbf{M} + \mathbf{A}(\omega)) - i\omega\mathbf{B}(\omega) + \mathbf{C} + \mathbf{K}_S & \mathbf{\Xi}^T \\ \mathbf{\Xi} & \mathbf{0} \end{bmatrix} \begin{bmatrix} \zeta \\ \mathbf{F}_J \end{bmatrix} = \begin{bmatrix} \mathbf{F}_E \\ \mathbf{0} \end{bmatrix} \quad (13)$$

The solution to Equation (13) yields the motion displacement ζ of the lump masses 1 to N_1+N_2, as well as the forces on the hinge $\mathbf{F}_J$. In the numerical simulations performed in this work, the rigid platform is divided into a finite number of segments and matrices $\mathbf{A}$ and $\mathbf{B}$ and vector $\mathbf{F_E}$ are computed in software Hydrostar. The motion displacement results for rigid and hinged structures are interpolated into a finer number of elements following [6].

C. Testing parameters

The testing parameters are described in this section. The motion and strain gauge response of the floating and rigid platform were tested in regular sea states. The range of tests are summarised in Table I. Wave amplitudes of h = 5 mm, 10 mm, 20 mm and 40 mm and frequencies of f = 0.4 to 1.6 Hz in steps of 0.1 Hz were tested. The tests were performed at an incidence angle of $\theta = 0°$.

TABLE I
RAO TESTS SPECIFICATIONS FOR TWO WAVE INCIDENCES $\theta = 0°$

H (mm)	f (Hz)	Type of platform
5	0.4-1.6	Rigid/Hinged
10	0.4-1.6	Rigid/Hinged
20	0.4-1.6	Rigid/Hinged
40	0.4-1.6	Rigid/Hinged

Defining the wave length as $\lambda = gT^2/2\pi$, the wave period as $T = 1/f$ and the length of the full platform

as L, we define the ratio of the wavelength to that of the length of the device, such that

$$\frac{\lambda}{L} = \frac{gT^2}{2\pi L}. \tag{14}$$

D. Measurement uncertainty

The experimental uncertainty from the Qualisys system is quantified by measuring the motion spheres of the platform at rest. The standard deviation is quantified and used as the experimental error of the motion system. An error of 1% is estimated for the motion detection system. The error of the strain gauge system is computed from the standard deviation of a measurement with the platform at rest. An average error of 2% is estimated for the strain gauges.

III. Results

In this Section, results for heave motion displacement are presented for the rigid and hinged platforms. Three different response regimes are identified: wave length longer than the platform ($\lambda/L > 2$), wave length near the length of the platform ($\lambda/L \approx 1$), and wave length shorter than the platform ($\lambda/L < 0.6$). Hence, results are presented for one representative case of each of these regimes.

A. Heave motion response

Motion displacement measurements, for both rigid and hinged platforms, are plotted in Figures 6a, 6c, 6e and Figures 6b, 6d, 6f, respectively, at $\lambda/L = 3.6$, $\lambda/L = 1.4$ and $\lambda/L = 0.5$, i.e. $\lambda/L > 2$, $\lambda/L \approx 1$ and $\lambda/L < 0.6$, respectively.

In the figures, the vertical and horizontal axes show the displacement normalised by the wave height Δz, and the horizontal coordinate along the platform x/l, respectively. In both Figure 6a and Figure 6b, Δz is plotted at h=5, 10, 20 and 40 mm with black, blue, red and magenta markers, respectively. The wave heights and their corresponding markers are indicated in the legend boxes of the second column of the figures. Numerical results are plotted with black solid lines.

A total of 12 finite x/l experimental data points are plotted in each figure. The markers correspond to the position of the motion detection spheres in the platform. We recall that each floating pontoon had four motion detection spheres located along their span, as shown in Figure 1. Error bars are plotted only for $h =$ 5 mm, for clarity of the figures.

Wave length longer than the platform ($\lambda/L > 2$): It can be seen that at $\lambda/L = 3.6$, both Figure 6a and Figure 6b show that the response of rigid and hinged platforms show similar trends. In fact, as shown in Figure 6a and Figure 6b, $\Delta z \approx 1$ throughout the full length of rigid and hinged platforms for the four tested wave heights (h=5, 10, 20 and 40 mm). The experimental and numerical results showed similar trends for the rest of the tests when $\lambda/L > 2$.

Wave length near the length of the platform ($\lambda/L \approx 1$): When the wave length is near the length of the platform, the response of both rigid and hinged platforms present a sagging shape. This is in agreement to previous numerical findings [1]. Figure 6c and Figure 6d show Δz measurements at $\lambda/L = 1.4$, as a representative example of the case when the wavelength is $\lambda/L \approx 1$.

It is observed, in Figure 6c, that the rigid platform shows a single sagging shape and maximum displacements occur at both of its free ends. In contrast, Figure 6d shows a triple sagging effect due to the presence of the two hinges. Results of the numerical model show a satisfactory agreement with the experimental results. We note that the curves start becoming asymmetric and with higher Δz towards the upstream side of the platforms (right hand side of Figure 6c and 6d), as the wavelength becomes shorter than the length of the platform.

Wave length shorter than the platform ($\lambda/L < 0.6$): When the wavelength is shorter than the platform, most of the vertical displacement Δz concentrates at the upstream side of the platform. This can be observed in Figures 6e and 6f for the rigid and the hinged platforms, respectively. Noteworthy, the motion of the hinged platform at the upstream side exceeds that of the rigid platform by approximately 50%. However, about 50% of the length of the hinged and rigid platforms remain with $\Delta z \leq 0.4$. Results highlight that when $\lambda/L < 0.6$, which represent sea states with high probability of occurrence [14], marine renewables could experience a reduced vertical displacement when located over $0 < x/l \leq 0.5$.

The discrepancies between experimental measurements and analytical model are attributed due to experimental uncertainty in the measurements. Furthermore, when $\lambda/L < 0.6$, the motion of the platform is more rapid and water goes overboard of the platform. This effect increases the spread of the experimental data and is not predicted in the numerical model. In the next section, we continue the analysis of spanwise and streamwise motion displacement of the platforms. Subsequently, we explore the loading response of the platforms.

B. Spanwise motion displacement of platforms

The spanwise deformation along the y-axis is studied in this Section. Figure 7 shows the contour plots of Δz, predicted numerically, as seen from a top view of the yx-plane of the platforms. The contours plots are shown over the range of $0.5 \leq \Delta z \leq 1.5$. The Δz contours of the rigid and hinged platforms are plotted on the left and right columns, respectively. The first, second and third rows correspond to $\lambda/L = 3.6$, $\lambda/L = 1.4$ and $\lambda/L = 0.5$, which are the same cases presented previously in Section III *A*.

In Figure 7, the normalised streamwise axis, x/l-axis, is plotted horizontally, whilst the normalised spanwise axis, y/l-axis, is plotted vertically. The experimental Δz is plotted in Figure 7 with black markers.

The contour plots shown in Figure 7, confirm the Δz motion trends, presented in Section III *A*, along

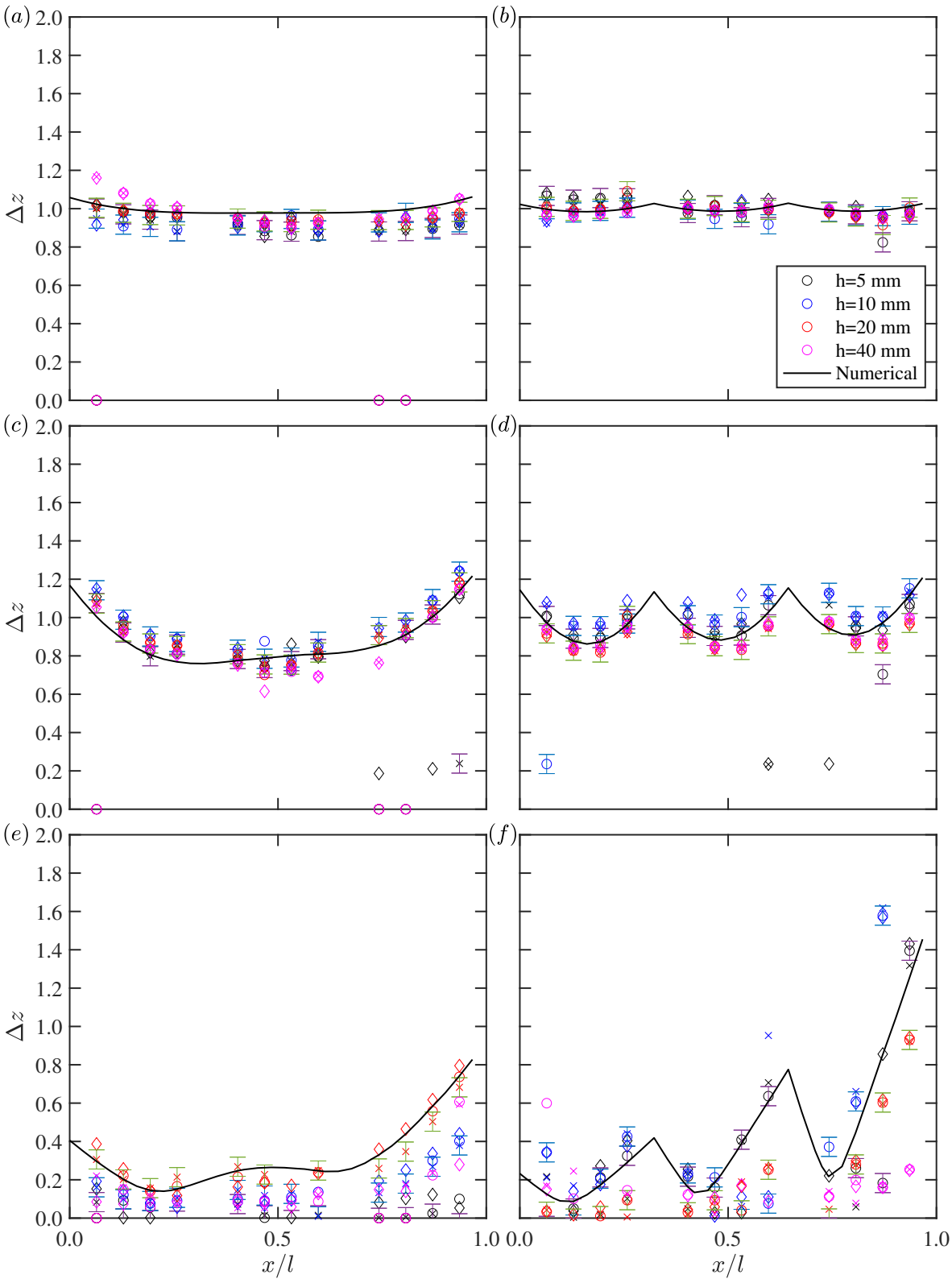

Fig. 6. Vertical displacement tests at $\lambda/L = 3.6$, $\lambda/L = 1.4$ and $\lambda/L = 0.5$, plotted in the first, second and third row, respectively, for the rigid ((a), (c), (e)) and hinged ((b), (d), (f)) structures.

the x-axis. Furthermore, the contour plots highlight that along the y-axis, Δz remains constant for all of the cases presented. This is also confirmed by the measured Δz, because the markers remain in most of the cases bold, as they are tracked along the y/l-axis. The constant spanwise (y/l) Δz predicted numerically and confirmed experimentally, highlight that for this type of material and wave forcing, the platform does not experience spanwise deformation (y/l), but only streamwise (x/l) deformation. This is a useful insight, when considering a depth distributed set of marine renewables along the y-axis. In the next Section, we study the characteristics of the streamwise deformation for both rigid and hinged platforms.

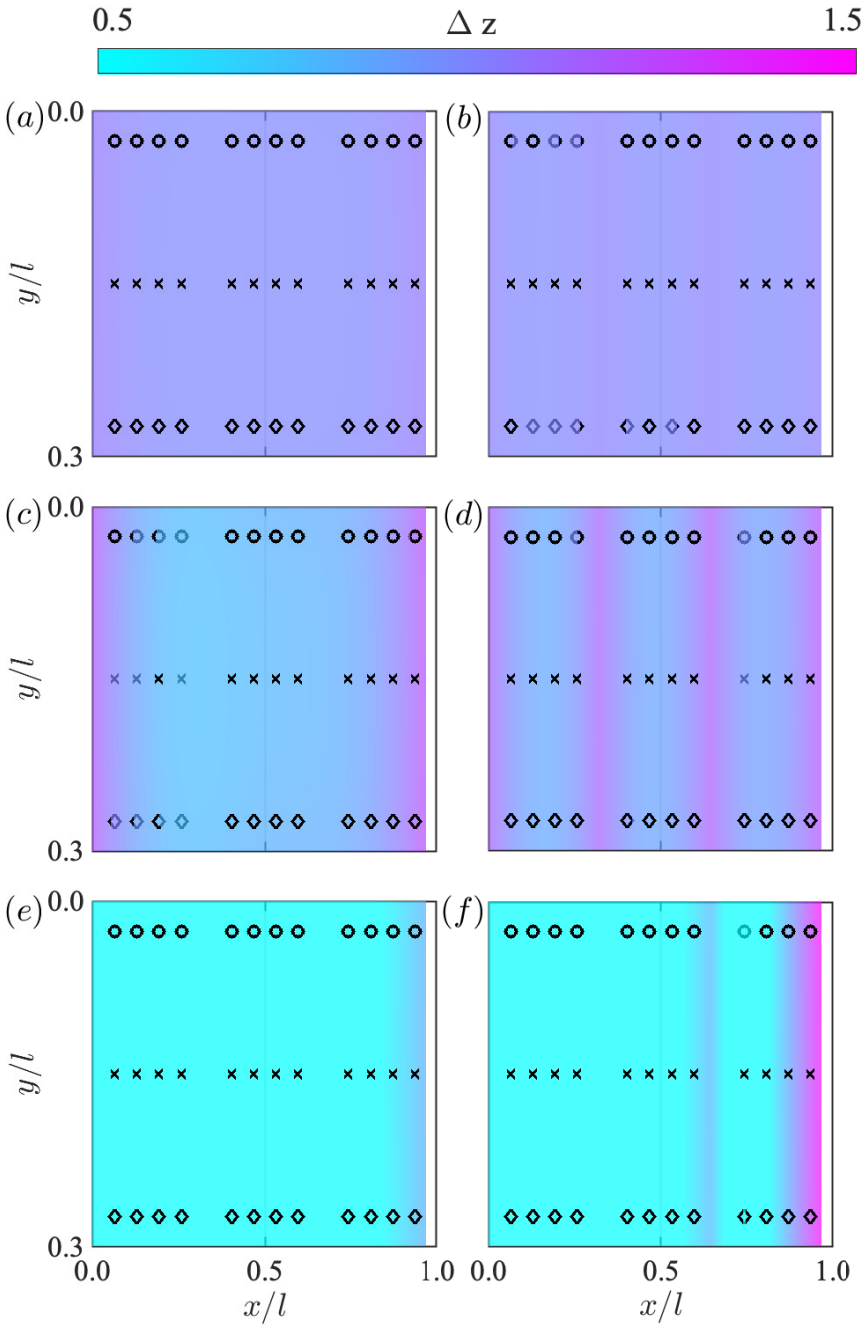

Fig. 7. Three dimensional vertical displacement at $\lambda/L = 3.6$, $\lambda/L = 1.4$ and $\lambda/L = 0.5$, plotted in the first, second and third row, respectively, of rigid (a),(c),(e) and hinged (b),(d),(f) structures.

C. Streamwise motion displacement of platforms

In this section, we compare the normalised motion amplitude Δz of different points along the x-axis of the floating platform to understand better which are the best locations to install marine renewable devices. We plot the numerical results and compare the results to the experimental measurements. We select three positions: closest to the upstream side of the platform, closest to the hinge and to the upstream side of the platform, and closest to the middle of the platform. We denote these positions as upstream, hinged and middle points.

Figure 8a and Figure 8b show the simulated motion response of the rigid and hinged platforms, respectively, for the upstream, hinged and middle points. Solid blue, red and black lines are used to plot the numerical results of the upstream, hinged and middle locations, respectively.

The experimental measurements of Δz, at the three different locations (upstream, hinged and middle points), are also plotted in both Figure 8a and Figure 8b, with the same color code used for the numerical results . The experimental data is plotted for h =5, 10 and 20 mm and for points located in the middle row of motion detection spheres shown in Figure 1.

Figure 8a shows that the middle and hinged points in the rigid platform have a similar behaviour. Specifically, Figure 8a shows that Δz grows from $\Delta z = 0$, when $\lambda/L = 0.4$, to an asymptotic value of $\Delta z = 1$, when $\lambda/L > 2.5$. In contrast, Δz of the upstream point

grows from $\Delta z = 0.5$ at $\lambda/L = 0.4$ to a maximum of $\Delta z = 1.2$ at $\lambda/L = 1$, and then drops and reaches an asymptotic value of $\Delta z = 1$, when $\lambda/L > 2.5$.

Figure 8b shows that for the hinged platform, the middle point of the platform behaves similarly to the middle point of the rigid platform. However, both hinged and upstream points behave differently, between $0.4 < \lambda/L > 1.4$. Specifically, in Figure 8b, both hinged and upstream points have peak amplitudes at approximately $\lambda/L > 0.6$ and $\lambda/L > 0.65$, respectively. Furthermore, the maximum motion amplitude at the hinged and upstream point is $\Delta z = 1.3$ and 1.7, respectively. Both of these maximums surpass the maximum Δz measured at the upstream point of the rigid platform. In contrast, when $\lambda/L > 2.5$, the hinged and upstream curves converge to $\Delta z = 1$, together with the middle point of the platform.

Hence, from the motion perspective, the hinged platform is less desirable than the rigid platform. Noteworthy, however, the middle point, in both rigid and hinged platforms, has a tendency to experience a reduced motion displacement when as $\lambda/L \approx 0.5$ and

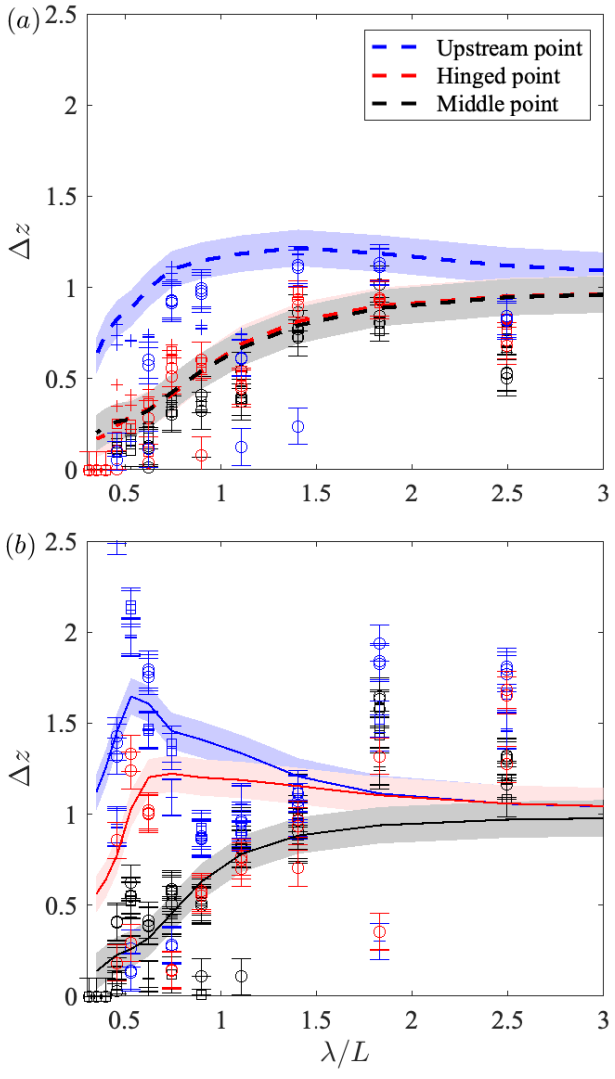

Fig. 8. Numerical RAO response for upstream, hinged and middle point of a) rigid and b) hinged platforms. Experimental measurements added for middle point.

therefore, could be used in both platforms to install marine renewables. In the next section, we study the vertical loads measured at the hinged position in both rigid and hinged platforms to quantify experimentally any load alleviation provided by the use of hinges in the floating platform.

D. Loading response of platforms

In the previous Section, we studied the motion response amplitude at different points in the rigid and hinged platforms. We observed that the hinged platform has larger maximum displacements at the hinge and upstream points in comparison to the maximum displacements of the rigid platform in the same locations. In this Section, we aim to understand the vertical loading response of the platforms through strain gauge measurements.

We compare the measurements of different strain gauges at each side of the rigid bar and hinge, for both, rigid and hinged structures, respectively. We denote these measurements as SG1, SG2, SG3 and SG4, Note that SG1 and SG2 are located at the upstream hinge/bar, and that SG1 is closer to the upstream side. Then, SG3 and SG4 are located at the downstream hinge/bar, and SG4 is closer to the downstream side. We recall, that force uncertainty for these measurements is quantified as the average of the standard deviation of the strain gauge signals measured in calm water. The uncertainty was approximately 2%.

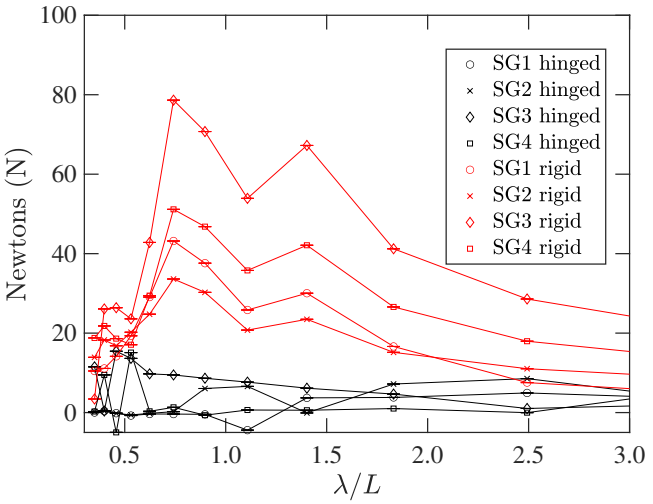

Fig. 9. Vertical force in Newtons measured by SG1, SG2, SG3, SG4, versus frequency at h=10 mm.

Figure 9 shows the forces measured with SG1, SG2, SG3 and SG4 for the rigid and hinged structures, in red and black, respectively. The results are plotted for wave loads measured at h = 10 mm. It can be seen that in all of the strain gauges, the measured vertical force is higher in the rigid structure (red markers) than in the hinged structure (black markers). In fact, the measured force in the hinged structure almost vanishes due to the presence of the hinges.

In particular, a region of high loading is identified in the rigid structure. The region between

$0.7 \geq \lambda/L \geq 1.4$, which is the region where $\lambda/L \approx 1$. Therefore, it can be seen that the hinge platform mitigates extreme loading of the rigid platform and is suitable for extending the fatigue life of the structure for the wider range of frequencies that could occur in the offshore environment.

E. Effect of Young's modulus on motion response of rigid platform

Lastly, the rigidity of the material used to manufacture the floating structure plays an important role in Δz. In particular, the stiffness matrix K_S changes due to the different Young's modulus of different materials. In this Section, we show the numerical computation of Δz of the rigid platform with three different values of Young's modulus. We show low, intermediate and high Young's modulus, i.e. low, intermediate and high stiffness materials. The high, medium and low Young's modulus could be representative of offshore steel, carbon fibre coupled with foam and a rubber like material, respectively.

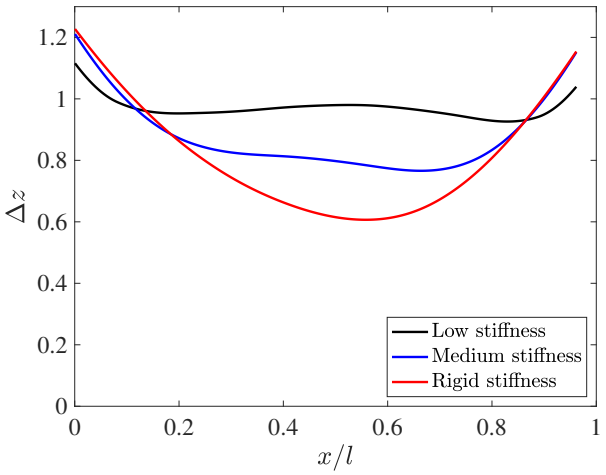

Fig. 10. Motion response Δz of rigid platform with low, medium and rigid Young's modulus plotted in black, blue and red, respectively.

Figure 10 shows the results of the simulations for Δz with different rigidity of materials. The horizontal axis shows the normalised length of the rigid platform x/l, whilst the vertical axis shows Δz. The red line shows a platform made with a rigid material (offshore steel). The blue line shows a platform built with carbon fibre and foam, as the platform tested in this work. The black line shows a low stiffness material (rubber like material). It can be seen that the rigid material sags more noticeably than the materials with lower stiffness. In contrast, for the low stiffness material, or flexible material, $\Delta z \approx 1$ between $0.1 \leq x/l \leq 0.9$. This type of low stiffness material, could also mitigate local minima along the structure. However, the investigation of flexible materials is topic of further research by the authors of this paper.

IV. Discussion

The applicability of the platforms studied in this paper are discussed in this section, towards their use as novel floating platforms for marine renewable energy. Floating platform such as the ones presented here, offer the possibility of deploying marine renewable devices in deep water, and offer the possibility of including more than one device per platform. Examples of floating marine renewable energy devices that could be deployed are, but not limited to: both horizontal and vertical tidal turbines [15], [16] and wave cycloidal rotors [14], [17]. Furthermore, hinged floating platforms can be used to extract energy through hinge motion [18].

The flexibility of the structure for towing and maneuvering offers the possibility of having a few of them in different parallel configurations, in which the wake of the devices have positive interference or minimise negative interference for devices that are not in the frontal row of the array.

To circumvent the difficulty of high loading in a large fixed floating structure, here, we demonstrate experimentally that the loading in the structure can be alleviated through the use of hinges. We also note that hinge motion can also be representative of the behaviour of a structure made with flexible materials [19], however, this is subject to further research by the authors of this paper.

V. Conclusions

In this paper, we study the motion and loading response of very large hinged floating platforms experimentally and numerically, to understand whether they could carry multiple marine renewable energy converters in a safe and reliable manner. To this aim, we analysed the performance of a hinged and rigid floating platform in terms of displacement and vertical loading.

The motion response showed three different behavioural regimes. Namely, wavelength longer than the platform ($\lambda/L > 2$), wavelength near the length of the platform ($\lambda/L \approx 1$) and wavelength shorter than the platform ($\lambda/L < 0.6$). When $\lambda/L > 2$ and $\lambda/L < 0.6$, the response of the rigid and floating platform behaved similarly.

When $\lambda/L > 2$, both rigid and hinged platforms show $\Delta z \approx 1$ throughout the full length of the structures. When $\lambda/L < 0.6$, the motion displacement concentrates at the upstream side of the platform. In contrast, when $\lambda/L \approx 1$, the hinged platform presents a triple sagging shape, whilst the rigid platform presents a single sagging response. These findings are in agreement with numerical results presented in [1], [20].

The vertical force analysis showed that a significant reduction in vertical loading is obtained in the hinged platform. In particular, this load reduction is more notorious when $0.7 \geq \lambda/L \geq 1.4$. Because approximately 50% of the length of the hinged platform remains at $\Delta z \leq 0.4$ when $\lambda/L < 0.6$, it is envisioned that hinged platforms can be used to deploy multiple marine renewables, subject to reduced vertical motion, whilst retaining the structural advantage of reduced internal loading.

Future studies include the experimental study of the hinged platform subject to irregular waves and different wave incidence angles, as well as the analytical and numerical analysis of the performance of tidal and wind turbines mounted in the hinged platforms.

ACKNOWLEDGEMENT

The authors would like to thank Dr Yibo Liang for the insightful discussions at the beginning of this work and PhD student Yi Huang for his help during the experiments carried out for this manuscript. Also to the staff of the Kelvin Hydrodynamics Lab: Grant, Bill and Steven, who manufactured and instrumented the hinged and rigid floating platforms.

REFERENCES

[1] X. Zhang, D. Lu, Y. Liang, and F. Brennan, "Feasibility of very large floating structure as offshore wind foundation: Effects of hinge numbers on wave loads and induced responses," *Journal of Waterway, Port, Coastal, and Ocean Engineering*, vol. 147, no. 3, p. 04021002, 2021.

[2] L. Li, "Full-coupled analysis of offshore floating wind turbine supported by very large floating structure with consideration of hydroelasticity," *Renewable Energy*, vol. 189, pp. 790–799, 2022.

[3] S. Li and F. Brennan, "Feasibility assessment of very large floating structures for offshore wind: Structural perspective," https://ssrn.com/abstract=4417894.

[4] S. Fu, T. Moan, X. Chen, and W. Cui, "Hydroelastic analysis of flexible floating interconnected structures," *Ocean Engineering*, vol. 34, no. 11, pp. 1516–1531, 2007.

[5] Y. Sun, D. Lu, J. Xu, and X. Zhang, "A study of hydroelastic behavior of hinged vlfs," *International Journal of Naval Architecture and Ocean Engineering*, vol. 10, no. 2, pp. 170–179, 2018.

[6] X. Zhang, D. Lu, Y. Gao, and L. Chen, "A time domain discrete-module-beam-bending-based hydroelasticity method for the transient response of very large floating structures under unsteady external loads," *Ocean Engineering*, vol. 164, pp. 332–349, 2018.

[7] D. Lu, S. Fu, X. Zhang, F. Guo, and Y. Gao, "A method to estimate the hydroelastic behaviour of vlfs based on multi-rigid-body dynamics and beam bending," *Ships and Offshore Structures*, vol. 14, no. 4, pp. 354–362, 2019.

[8] Y. Chen, X. Zhang, L. Liu, X. Tian, X. Li, and Z. Cheng, "A discrete-module-finite-element hydroelasticity method in analyzing dynamic response of floating flexible structures," *Journal of Fluids and Structures*, vol. 117, p. 103825, 2023. [Online]. Available: https://www.sciencedirect.com/science/article/pii/S0889974622002171

[9] Y. Chen, X. Zhang, K. Shen, and X. Ren, "Extension of the discrete-module-finite-element method into the interconnected large floating flexible structures," *Ocean Engineering*, vol. 269, p. 113549, 2023. [Online]. Available: https://www.sciencedirect.com/science/article/pii/S0029801822028323

[10] I. Noad and R. Porter, "Modelling an articulated raft wave energy converter," *Renewable Energy*, vol. 114, pp. 1146–1159, 2017.

[11] M. E. McCormick, *Ocean Wave Energy Conversion*, first edition. ed. Dover Publications, Inc., 2007.

[12] J.-S. Yoon, S.-P. Cho, R. G. Jiwinangun, and P.-S. Lee, "Hydroelastic analysis of floating plates with multiple hinge connections in regular waves," *Marine Structures*, vol. 36, pp. 65–87, 2014.

[13] X. Zhang and D. Lu, "An extension of a discrete-module-beam-bending-based hydroelasticity method for a flexible structure with complex geometric features," *Ocean Engineering*, vol. 163, pp. 22–28, Sep 2018.

[14] A. Arredondo-Galeana, G. Olbert, W. Shi, and F. Brennan, "Near wake hydrodynamics and structural design of a single foil cycloidal rotor in regular waves," *Renewable Energy*, vol. 206, pp. 1020–1035, 2023. [Online]. Available: https://www.sciencedirect.com/science/article/pii/S0960148123002124

[15] A. Arredondo-Galeana and F. Brennan, "Floating offshore vertical axis wind turbines: Opportunities, challenges and way forward," *Energies*, vol. 14, no. 23, 2021.

[16] A. Arredondo-Galeana, A. M. Young, A. S. Smyth, and I. M. Viola, "Unsteady load mitigation through a passive trailing-edge flap," *Journal of Fluids and Structures*, vol. 106, p. 103352, 2021.

[17] A. Arredondo-Galeana, A. Ermakov, W. Shi, J. V. Ringwood, and F. Brennan, "Control strategies for power enhancement and fatigue damage mitigation of wave cycloidal rotors."

[18] C. P. Cummins, G. T. Scarlett, and C. Windt, "Numerical analysis of wave–structure interaction of regular waves with surface-piercing inclined plates," *Journal of Ocean Engineering and Marine Energy*, vol. 8, no. 1, pp. 99–115, Feb 2022. [Online]. Available: https://doi.org/10.1007/s40722-021-00219-6

[19] S. Brown, N. Xie, M. Hann, and D. Greaves, "Investigation of wave-driven hydroelastic interactions using numerical and physical modelling approaches," *Applied Ocean Research*, vol. 129, p. 103363, 2022. [Online]. Available: https://www.sciencedirect.com/science/article/pii/S0141118722002942

[20] Y. Chen, Y. Zhang, X. Tian, X. Guo, X. Li, and X. Zhang, "A numerical framework for hydroelastic analysis of a flexible floating structure under unsteady external excitations: Motion and internal force/moment," *Ocean Engineering*, vol. 253, p. 111288, 2022. [Online]. Available: https://www.sciencedirect.com/science/article/pii/S0029801822006825